ADVANCED ENERGY MATERIALS
www.advenergymat.de

A Series of Ternary Metal Chloride Superionic Conductors for High-Performance All-Solid-State Lithium Batteries

Jianwen Liang, Eveline van der Maas, Jing Luo, Xiaona Li, Ning Chen, Keegan R. Adair, Weihan Li, Junjie Li, Yongfeng Hu, Jue Liu, Li Zhang, Shangqian Zhao, Shigang Lu, Jiantao Wang, Huan Huang, Wenxuan Zhao, Steven Parnell, Ronald I. Smith, Swapna Ganapathy, Marnix Wagemaker, and Xueliang Sun**

Understanding the relationship between structure, ionic conductivity, and synthesis is the key to the development of superionic conductors. Here, a series of $Li_{3-3x}M_{1+x}Cl_6$ ($-0.14 < x \leq 0.5$, M = Tb, Dy, Ho, Y, Er, Tm) solid electrolytes with orthorhombic and trigonal structures are reported. The orthorhombic phase of Li–M–Cl shows an approximately one order of magnitude increase in ionic conductivities when compared to their trigonal phase. Using the Li–Ho–Cl components as an example, their structures, phase transition, ionic conductivity, and electrochemical stability are studied. Molecular dynamics simulations reveal the facile diffusion in the *z*-direction in the orthorhombic structure, rationalizing the improved ionic conductivities. All-solid-state batteries of NMC811/$Li_{2.73}Ho_{1.09}Cl_6$/In demonstrate excellent electrochemical performance at both 25 and −10 °C. As relevant to the vast number of isostructural halide electrolytes, the present structure control strategy guides the design of halide superionic conductors.

1. Introduction

The development of high-performance all-solid-state batteries is contingent on the finding and synthesis of solid-state electrolytes (SSEs) with high ionic conductivity, good chemical stability, wide electrochemical windows, and desirable mechanical properties.[1–4] Recently, several families of SSEs have attracted significant interest, such as sulfides or oxides with polyanionic frameworks (PS_4^{3-}, PO_4^{3-}, etc.) and halides with close-packed anion sublattice structures.[5–10] Among these candidates, a promising family of metal chloride SSEs generally possess a wide electrochemical stability window (≈4 V), and good chemical stability toward ambient air and cathode materials (e.g., $LiCoO_2$).[11–14] Some of them can be even synthesized at large scales from aqueous solutions.[6] Although chloride-based SSEs have been developed over the past decades,[15–18] their use has been limited due to their low ionic conductivities. Recently, due to the development of superionic conductor such as Li_3YCl_6[14] and Li_3InCl_6,[19,20] metal halide SSEs have received renewed attention.[21–34] Until now, only a few metal chloride SSEs have achieved high room-temperature (RT) ionic conductivities over 10^{-3} S cm^{-1}, including Li_3InCl_6,[19,20] Zr-doped Li_3MCl_6 (M = Y, Er, Yb, In),[21,26,27,33] $Li_3Y_{1-x}In_xCl_6$,[22] Li_xScCl_{3+x},[23] $Li_2Sc_{2/3}Cl_4$,[24] etc. In the search for new metal chloride SSEs, a better understanding of the relationship between structure and ionic conductivity is highly demanded.[19,35–37]

Ternary chlorides with the composition of $Li_3M(III)Cl_6$, where M(III) represents a trivalent rare earth metal, can crystallize in three types of structures including monoclinic (*C2/m*), trigonal (*P-3m1*), and orthorhombic (*Pnma*) phase.[6,18] Because the ionic radius of Cl^- is typically much larger than that of the rare earth M^{3+} ions, the Cl^- sublattice forms the

J. Liang, J. Luo, X. Li, K. R. Adair, W. Li, J. Li, X. Sun
Department of Mechanical and Materials Engineering
University of Western Ontario
1151 Richmond St, London, Ontario N6A 3K7, Canada
E-mail: xsun9@uwo.ca

E. van der Maas, W. Zhao, S. Parnell, S. Ganapathy, M. Wagemaker
Department of Radiation Science and Technology
Delft University of Technology
Delft 2629 JB, The Netherlands
E-mail: M.Wagemaker@tudelft.nl

N. Chen, Y. Hu
Canadian Light Source
44 Innovation Boulevard, Saskatoon, SK S7N 2V3, Canada

The ORCID identification number(s) for the author(s) of this article can be found under https://doi.org/10.1002/aenm.202103921.

DOI: 10.1002/aenm.202103921

J. Liu
Neutron Scattering Division
Oak Ridge National Laboratory
Oak Ridge, TN 37831, USA

L. Zhang, S. Zhao, S. Lu, J. Wang
China Automotive Battery Research Institute Co. Ltd
5th Floor
No. 43
Mining Building
North Sanhuan Middle Road, Beijing 100088, China

H. Huang
Glabat Solid-State Battery Inc.
700 Collip Circle, London, ON N6G 4×8, Canada

R. I. Smith
ISIS facility
Rutherford Appleton Laboratory
Harwell Campus, Didcot OX11 0QX, UK

framework of these structures, where the interstitial sites are occupied by the Li^+ and M^{3+} ions. The monoclinic structure occurs with relatively small metal radii, such as In or Sc. The Cl^- sublattice forms a cubic close packing (ccp) stacking. In both the trigonal and orthorhombic structures, the Cl^- sublattice is stacked in a hexagonal close packing (hcp) fashion. The hcp halogen stacking is interesting as it provides 6 octahedral and 12 tetrahedral interstitial sites in the Cl^- sublattice per formula unit, with only 4 cations to occupy them. The specific cation and vacancy arrangements imposed by the different symmetry of the trigonal and orthorhombic structures can be expected to result in distinct Li^+ migration. In the competition between the hcp stacked trigonal and orthorhombic structures, the average metal radius has been suggested to play a decisive role,[6] where the structures crystallize in the *Pnma* space group with smaller M^{3+} ions (Yb, Lu) and *P-3m1* the space group with larger M^{3+} ions (Tb, Dy, Ho, Er, Tm) at RT. Only Li_3YCl_6 has been reported in both space groups, while its *Pnma* phase is metastable at RT. That was explained by an order–disorder phase transition connecting the two phases, with a phase transition temperature close to RT.[18]

In this work, we investigate the interplay between composition, structure, and Li-ion conductivity through the preparation of a series of Li–M(III)–Cl SSEs. Using Li–Ho–Cl as an example, a new series of orthorhombic-structured $Li_{3-3x}Ho_{1+x}Cl_6$ ($0.04 < x \leq 0.2$, where x is calculated based on the ratio between LiCl and $HoCl_3$ from the synthesis process) were synthesized for the first time. These orthorhombic Li–Ho–Cl materials show a cold-pressed ionic conductivity up to 1.3×10^{-3} S cm^{-1} at RT. That is over fourfold greater than that of the Li_3HoCl_6 ($x = 0$) with a trigonal structure (*P-3m1*). The all-solid-state batteries with an In/Li–Ho–Cl/NMC811 configuration demonstrate excellent electrochemical performance at RT and −10 °C. A detailed structural investigation is combined with molecular dynamics simulations to reveal the relationship between structure and Li-ion conductivity. Moreover, a similar trigonal-to-orthorhombic phase transition is reproducible in all Li–M(III)–Cl (M = Y, Er, Dy, Tm) structures but not in the Li–Tb–Cl system. About one order of magnitude difference in ionic conductivities is observed in the isostructural Li–Dy–Cl, Li–Y–Cl, Li–Er–Cl, and Li–Tm–Cl compositions. The increase in ionic conductivity from the trigonal to the orthorhombic phase is rationalized by the fact that the orthorhombic phase results in easier Li^+ transport along the *c*-lattice direction, which is a critical step in the diffusion network. The rare-earth abundance is a significant issue from a practical perspective. The cost of exploring and synthesizing Li^+ conductors of Li–M–Cl here may be high within a short time, but once the discovery of new high-performance materials, further efforts can be made to satisfy the industrial cost targets. The broadening of the promising halide SSEs based on the new chemistry insights provided in this work will also promote the development of more halide SSEs to make them closer to realistic application for sure. These new insights into the relationship of ionic conductivity, chemical composition, and structure provide a new opportunity for halide solid electrolytes design and for the ultimate pursuit of highly conductive, stable, and processable solid electrolytes as required for all-solid-state batteries.

2. Results

2.1. Influence of Synthesis on the Structure of Li-Ho-Cl Halide SSEs

The Li–Ho–Cl halide SSEs were synthesized from a stoichiometric mixture of LiCl and $HoCl_3$ precursors directly by comelting at 650 °C for 24 h. As presented in the X-ray diffraction (XRD) patterns of $Li_{3-3x}Ho_{1+x}Cl_6$ materials (**Figure 1**a,b and Figure S1, Supporting Information, x is calculated based on the nominal stoichiometry between LiCl and $HoCl_3$), when x is lower than 0.02, such as $Li_{2.95}Ho_{1.017}Cl_6$ (Figure S1, Supporting Information, $x = 0.017$), Li_3HoCl_6 (Figure 1a, $x = 0$), and $Li_{3.42}Ho_{0.86}Cl_6$ (Figure 1a, $x = -0.14$), the products can be indexed to a trigonal structure of Li_3HoCl_6 with the space group of *P-3m1* (ICSD No. 04-009-8880).[18] Neutron powder diffraction (NPD) and Rietveld refinement of the Li_3HoCl_6 (Figure 1c) further confirmed the trigonal structure. The unit cell of Li_3HoCl_6 sample contains eight crystallographic atom positions (Cl1, Cl2, Cl3, Li1, Li2, Ho1, Ho2, Ho3) as shown in Table S1 of the Supporting Information. There is a slight difference in the occupations of the Ho1 and Ho2 sites when compared to the reported trigonal phase of Li_3HoCl_6. When the value of x is in the range from 0.04 to 0.2, $Li_{3-3x}Ho_{1+x}Cl_6$ crystallized in a different structure (Figure 1b; Figure S1, Supporting Information). The XRD patterns of $Li_{2.4}Ho_{1.2}Cl_6$ ($x = 0.2$), $Li_{2.73}Ho_{1.09}Cl_6$ ($x = 0.09$), and $Li_{2.87}Ho_{1.043}Cl_6$ ($x = 0.043$) reveal that the new phase has a similar orthorhombic structure to Li_3YbCl_6 (ICSD No. 04-009-8883).[18] The structure of the *Pnma* phase was further confirmed by NPD Rietveld refinement of the three highest resolution detector banks (Figure 1d; Figures S2, and S3, Supporting Information) of the material $Li_{2.73}Ho_{1.09}Cl_6$ sample. Although the ratio of LiCl to $HoCl_3$ in the synthesis process is slightly lower than 3:1 (≈2.5 to 1), the refinement converged to the final stoichiometry of Li_3HoCl_6. The small amount of difference might be due to the trace amount of $HoCl_3$ impurity in the final product.

Both Li–Ho–Cl orthorhombic and trigonal structures are built up by hcp anion stacking, forming octahedral of six Cl^- with central Ho^{3+}, Li^+, or empty sites. The two phases differ in their arrangement of the cations (**Figure 2**a–c). In the orthorhombic *Pnma* structure, the unit cell has three octahedra sites: 4*c*, 8*d1*, and 8*d2* (Table S2, Supporting Information; Figure 2b). The 4*c* site is fully occupied by the Ho^{3+}. Both Li1 and Li2 are occupied in the 8*d* sites with occupancy parameters of 0.848 and 0.652, respectively. Each $HoCl_6^{3-}$ octahedron is surrounded by three edge-sharing $LiCl_6^{5-}$ octahedra with a short Ho–Li distance (Figure 2d,e). In the trigonal structure, there are three Ho sites (Figure 2c). One is fully occupied (Ho1, 1*a* site) and the other two are partially occupied. There are two Li sites, the fully occupied Li1 layer (6*g* site) and half occupied Li2 layer (6*d* site) along the *c*-direction. Each $HoCl_6^{3-}$ octahedron is surrounded by six edge-shared $LiCl_6^{5-}$ octahedra, forming a honeycomb lattice in the *ab* plane (Figure 2g,h). The trigonal structure contains infinite chains of face-sharing $HoCl_6^{3-}$ octahedra in the [001] direction. The local structure of the $HoCl_6^{3-}$ octahedron is also different between the two structures (Figure 2f,i). Specifically, the asymmetric local environment induces a distorted Cl^- arrangement around Ho (Figure 2f) in orthorhombic Li_3HoCl_6.

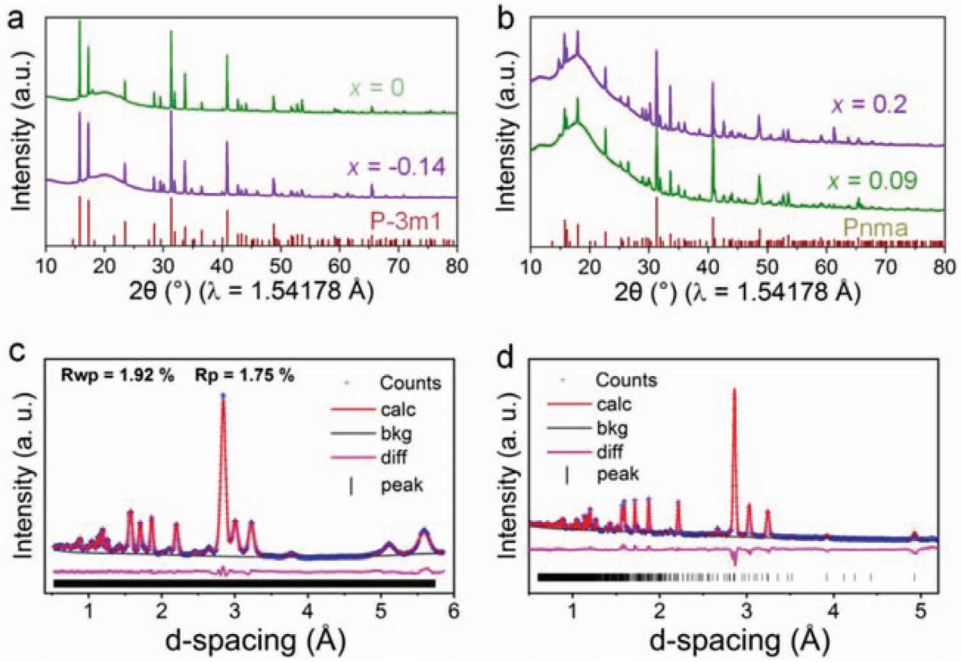

Figure 1. XRD and neutron diffraction patterns of the Li–Ho–Cl system. a) XRD patterns of Li_3HoCl_6 ($x = 0$) and $Li_{3.42}Ho_{0.86}Cl_6$ ($x = -0.14$) samples. Both patterns were indexed to the same space group of *P-3m1*. b) XRD patterns of $Li_{2.4}Ho_{1.2}Cl_6$ ($x = 0.2$) and $Li_{2.73}Ho_{1.09}Cl_6$ ($x = 0.09$) samples. The patterns were indexed to the same space group of *Pnma*. Fitted time-of-flight NPD patterns of c) the Li_3HoCl_6 sample, d) the $Li_{2.73}Ho_{1.09}Cl_6$ sample and the fit resulting from the Rietveld refinement.

Holmium L_3-edge X-ray absorption fine structure (XAFS) was employed to reveal the detailed structures of the Li–Ho–Cl SSEs (**Figure 3**a; Figures S4 and S5, Supporting Information). There are four different characteristic peaks (marked as *a*, *b*, *c*, and *d*) in the X-ray absorption near edge structure (XANES) spectra of the *Pnma* phase $Li_{2.73}Ho_{1.09}Cl_6$ and *P-3m1* phase Li_3HoCl_6 samples. The difference of the Ho local environment between *Pnma* and *P-3m1* phases comes from a slight distortion of the $HoCl_6^{3-}$ octahedron in the *Pnma* phase and different arrangements of cations in the second shell which is related to the Li and vacancy sites (Figure 3f, dark green points). Figure 3b–d shows the overall $k\chi(k)$, back Fourier transform (BFT) filtered $k\chi(k)$ for the 1st shell FT, and BFT filtered $k\chi(k)$ for the 2nd shell FT of the $Li_{2.73}Ho_{1.09}Cl_6$ (*Pnma*) sample, respectively. Close agreement is achieved between the experimental data and Feff modeling[38] for the Ho centered spherical cluster (R = 6 Å, Figure 3f), thus the initial Feff modeling supports the Ho local structural environment in the $Li_{2.73}Ho_{1.09}Cl_6$ (*Pnma*) sample. The Ho centered spherical cluster was developed up to 5.5 Å, covering Ho local structure environment up to the 2nd FT peak (Figure S6, Supporting Information). A five-path structure model for R space curve fitting was developed with scattering paths from corresponding coordination shells predicted by the theoretical *Pnma* structure of Li_3HoCl_6 to degenerate into five individual scattering paths (Table S3, Supporting Information). The calculated coordination number (CN) and bond distances were used to guide the R space curve fitting.[39] Table S3 of the Supporting Information shows the structure parameters comparison between the R space curve fitting result and the *Pnma* Li_3HoCl_6 model. Figures S7 and S8 of the Supporting Information compared the experimental data and Feff modeling in FT and $k^3\chi(k)$. It can be concluded that the R space curve fitting is well consistent with the initial Feff modeling. The Finite Difference Method for Near-Edge Structure modeling[39] was performed to develop the corresponding theoretical XANES based on the same cluster. Comparison is made between the modeling and experimental data in XANES and their first derivative spectra (Figure 3e), revealing good agreement. The modeling data in k space for $k\chi(k)$ (Figure S9, Supporting Information) is also consistent with the initial Feff modeling (Figure 3b). Thus, the Ho occupation at octahedral sites of the $Li_{2.73}Ho_{1.09}Cl_6$ was proven by the initial Feff modeling, R space curve fitting, and XANES theoretical modeling, further verifying the structural models derived from XRD and neutron diffraction data.

2.2. The Influence of Synthesis on the Ionic Transport

Ionic conductivities of the cold-pressed $Li_{3-3x}Ho_{1+x}Cl_6$ SSEs were measured by temperature-dependent alternating-current impedance. The conductivity plateau at 25 °C corresponds to $\approx 1.3 \times 10^{-3}$ S cm^{-1} is associated with the long-range ion transport as shown in the conductivity isotherms in **Figure 4**a. The 3D ionic transport in $Li_{2.73}Ho_{1.09}Cl_6$ is reflected by the dispersive regime at a higher frequency at –15 °C with a κ value of 0.67 according to the Jonscher's power law[40,41] ($\sigma(\nu) \propto \nu^{\kappa}$). Figure 4b shows the comparison of representative Nyquist plots at 25 °C for the $Li_{2.73}Ho_{1.09}Cl_6$ (*Pnma*) and the Li_3HoCl_6 (*P-3m1*). The equivalent circuit (Figure 4b) consists of one parallel constant phase element (CPE)/resistor (R) in series with a CPE. The ideality CPE for the parallel combination

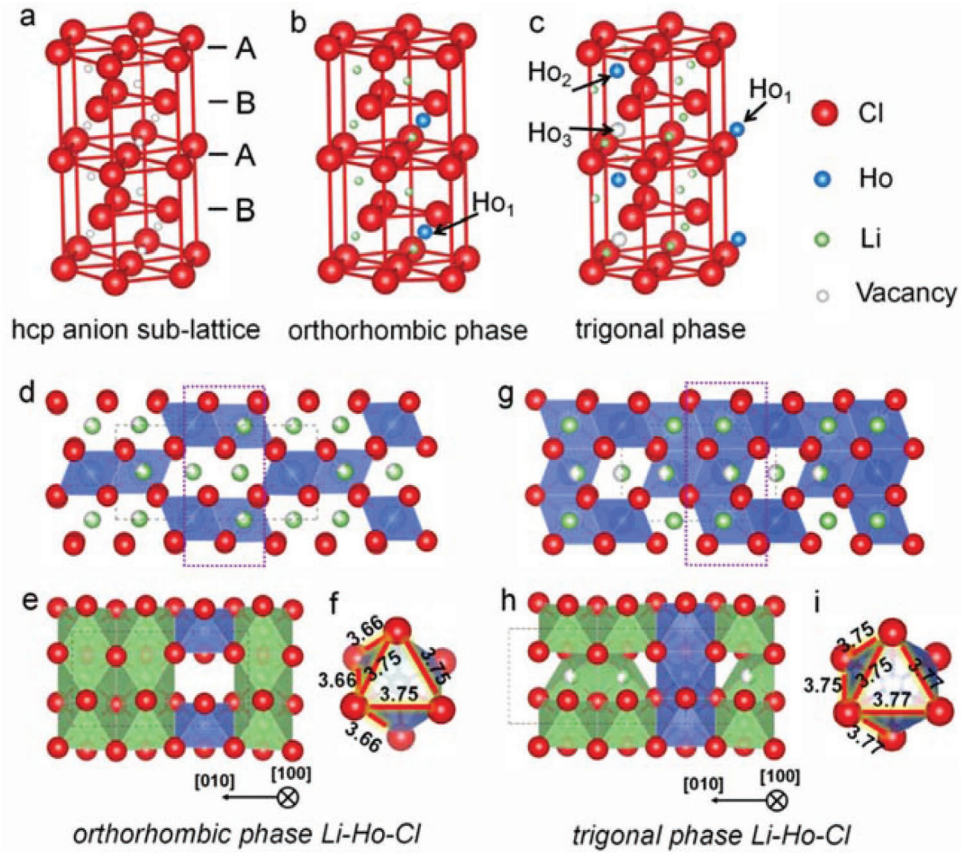

Figure 2. The structure and anion/cation arrangements of orthorhombic and trigonal structures of Li_3HoCl_6. a–c) The different cation arrangements of Ho and vacancy sites in orthorhombic and trigonal structures. d,e) Orthorhombic structure of the Li_3HoCl_6 unit cell. f) The $HoCl_6^{3-}$ octahedron in the orthorhombic phase of Li_3HoCl_6. g,h) Trigonal structure of the Li_3HoCl_6 unit cell. i) The $HoCl_6^{3-}$ octahedron in the trigonal phase of Li_3HoCl_6. Green, Li; Blue, Ho; Red, Cl.

CPE/R can be concluded from the estimated ideality factor α of 0.876 and 0.868 for the $Li_{2.73}Ho_{1.09}Cl_6$ and Li_3HoCl_6, respectively.[42] Moreover, the bulk transport characteristics of these SSEs can be reflected from their geometric capacitance C values (49.58 pF cm^{-2} for $Li_{2.73}Ho_{1.09}Cl_6$ and 47.83 pF cm^{-2} for Li_3HoCl_6).[43] Arrhenius plots and the extracted activation energies (E_a) with RT ionic conductivities of all $Li_{3-3x}Ho_{1+x}Cl_6$ are presented in Figure 4c,d.

For the *Pnma* structures ($0.04 < x \leq 0.2$), the RT ionic conductivities gradually increase with decreasing x, where the maximum ionic conductivity of 1.3×10^{-3} S cm^{-1} is obtained at $x = 0.09$. The ionic conductivity decreases dramatically when decreases further to $x = 0.02$. As aforementioned, $Li_{3-3x}Ho_{1+x}Cl_6$ changes from *Pnma* to *P-3m1* when $x \leq 0.02$. Li_3HoCl_6 (*P-3m1*) exhibits an RT Li^+ conductivity of 2.9×10^{-4} S cm^{-1}. Moreover, the activation energies of the $Li_{3-3x}Ho_{1+x}Cl_6$ SSEs show the opposite trend (Figure 4d). An activation energy below 0.4 eV is achieved for $Li_{3-3x}Ho_{1+x}Cl_6$ SSEs with the *Pnma* phase, and the value notably increases with decreasing x for $Li_{3-3x}Ho_{1+x}Cl_6$ with the *P-3m1* phase. This indicates that the cation arrangement of the *Pnma* symmetry supports lower activation energy for Li^+ transport as compared to *P-3m1*. The electronic conductivity of $Li_{2.73}Ho_{1.09}Cl_6$ was determined to be less than 1×10^{-9} S cm^{-1} as measured by chronoamperometry (Figure S10, Supporting Information). At the same time, the stability of $Li_{3-3x}Ho_{1+x}Cl_6$ SSEs in dry air was evaluated by thermogravimetric analysis, differential scanning calorimetry (Figure S11, Supporting Information) test, and XRD measurements (Figures S12 and S13) after exposure in a lithium battery dry room for 24 h. The results confirm that $Li_{3-3x}Ho_{1+x}Cl_6$ SSEs are stable in dry air and can be exposed for hours in the lithium battery dry room, which facilitates practical application.

2.3. The Universal Trigonal-to-Orthorhombic Phase Transition Process

Moreover, it has been found that the trigonal-to-orthorhombic phase transition is universal in many other kinds of Li–M(III)–Cl SSEs except Li-Tb-Cl compositions (**Figure 5**; Figure S14, Supporting Information). Preliminary results indicate that *Pnma* phase may be a stabilized high temperature phase of the Li–M(III)–Cl system (Figure S15, Supporting Information). Though the metastable orthorhombic structure of Li_3YCl_6 has been previously reported,[6,18] it is the first time to achieve the orthorhombic phase for other Li–M(III)–Cl (M = Ho, Er, Dy, Tm) materials, which makes a more clear understanding of the chemistry and structure formation of ternary rare-earth chlorides. Meanwhile, the increased conductivity from the trigonal to the orthorhombic phase can be found in all $Li_{3-3x}M_{1+x}Cl_6$

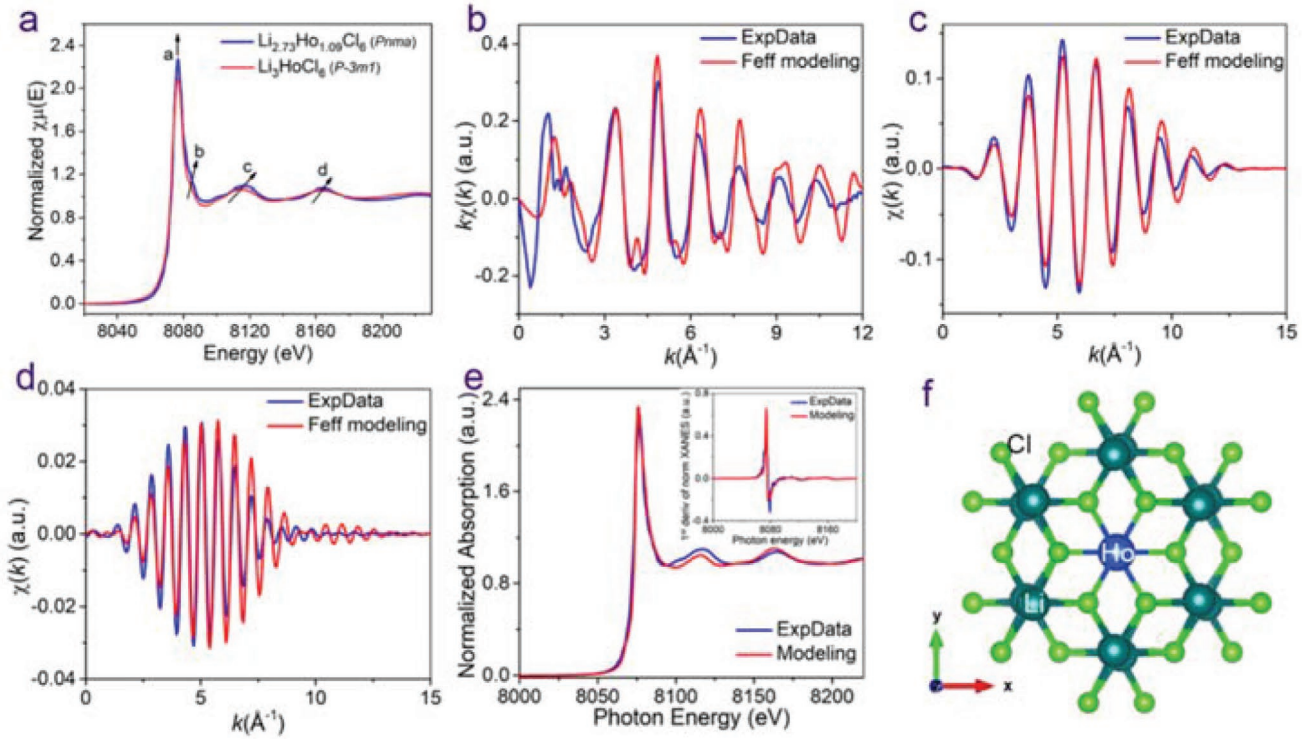

Figure 3. The local environment of Ho in the Li–Ho–Cl components based on XAFS fitting. a) Typical Ho L_3-edge XAFS spectra of *Pnma* phase $Li_{2.73}Ho_{1.09}Cl_6$ and *P-3m1* phase Li_3HoCl_6 samples. b) The overall $k\chi(k)$ between the experimental (blue line) and the Feff modeling (red line) of Ho local environment of $Li_{2.73}Ho_{1.09}Cl_6$ (*Pnma*). c) BFT filtered $k\chi(k)$ for the 1st shell FT of $Li_{2.73}Ho_{1.09}Cl_6$ (*Pnma*), sine function with window range: 1.3–2.8 Å. d) BFT filtered $k\chi(k)$ for the 2nd shell FT of $Li_{2.73}Ho_{1.09}Cl_6$ (*Pnma*), sine function with window range: 3.6–5.0 Å. e) Comparison between the experimental XANES (blue line) and the best fit of the XANES theoretical modeling (red line). f) The first and second shell of the Ho substructural system (Ho centered spherical cluster with a radius of R = 6 Å).

SSEs (Figure 5c). The $Li_{2.73}Dy_{1.09}Cl_6$, $Li_{2.73}Y_{1.09}Cl_6$, $Li_{2.73}Er_{1.09}Cl_6$, and $Li_{2.73}Tm_{1.09}Cl_6$ with orthorhombic phase possesses a high RT ionic conductivity of 9.0×10^{-4}, 7.0×10^{-4}, 6.4×10^{-4}, and 8.9×10^{-4} S cm^{-1}, respectively, which is about an order of magnitude high than their Li_3MCl_6 counterparts with trigonal structure. It is believed that the similar structural transition process and the induced conductivity evolution in many kinds of $Li_{3-3x}M_{1+x}Cl_6$ indicates a general phenomenon, which can be used to explore and achieve many new materials.

2.4. Computational Understanding of Ionic Conductivity

To understand the difference in ionic conductivities between the two structures, both phases were simulated by ab initio Molecular Dynamics for the composition of Li_3HoCl_6. The *Pnma* phase shows higher long-range diffusion, as illustrated in **Figure 6**a,b. The activation energies extracted from the slope of the Arrhenius plot are similar, but have a slight difference in the experimental observations (Figure 4). To further investigate the reason for the higher conductivity we consider the equation for the diffusion coefficient

$$D = gfv^0a^2 \exp\left(\frac{E_a}{k_bT}\right) = D_0 \exp\left(\frac{E_a}{k_bT}\right) \quad (1)$$

Here, g is the geometrical factor, f is the correlation factor, v^0 is the attempt frequency, and a is the jump distance, which can all be summarized into the preexponential factor D_0. The geometrical factor describes the effect of a porous network on diffusion. The correlation factor describes the percentage of back and forth movements of atoms between sites, and is defined as

$$f = \frac{D_{\text{Tracer}}}{D_{\text{jump}}} \quad (2)$$

where D_{Tracer} is the tracer diffusion coefficient and D_{jump} the jump-diffusion coefficient.

Both the attempt frequencies and the amplitudes of the Li^+ ions or Cl vibrations extracted by the Fourier transform of the diffusion paths[44] are similar in both phases (Figure S16, Supporting Information). The increase in ionic conductivity is therefore not due to an increase in attempt frequency. The influence of jump distance a (≈3.1Å) approximated by the distance between the different Wyckoff sites in both phases is also excluded. Hence, the difference observed in D_0 has to arise either from the geometrical factor or the correlation factor. The jumps between different Li sites under different temperatures are illustrated in Figure 6c,d and Figures S17–S20 (Supporting Information). The red lines represent jumps that occurred, with the thickness of the line indicating the frequency of the jump

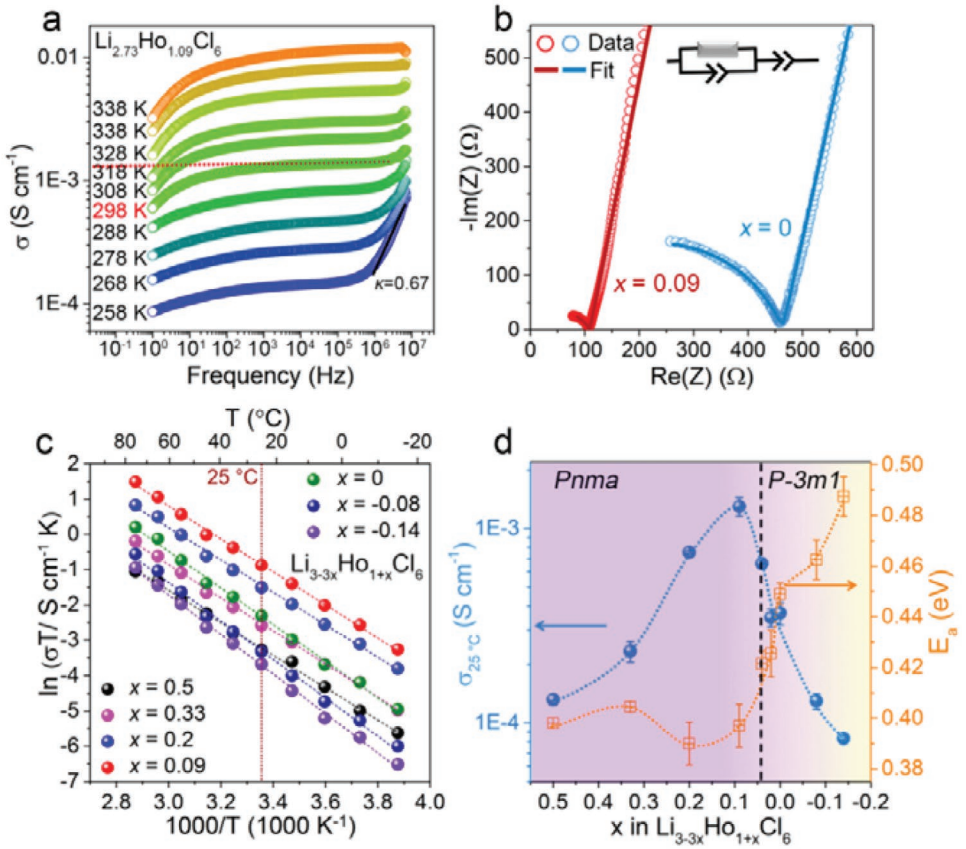

Figure 4. a) Conductivity isotherms $\sigma(\nu)$ of the as-prepared $Li_{2.73}Ho_{1.09}Cl_6$ SSE recorded at different temperatures. b) Representative Nyquist-plots for the as-prepared *Pnma* phase $Li_{2.73}Ho_{1.09}Cl_6$ and *P-3m1* phase Li_3HoCl_6 SSEs at 25 °C. c) Arrhenius-plots of the $Li_{3-3x}Ho_{1+x}Cl_6$ SSEs ($-0.14 \le x \le 0.5$). d) The RT ionic conductivities and corresponding activation energies of the $Li_{3-3x}Ho_{1+x}Cl_6$ SSEs ($-0.14 \le x \le 0.5$).

occurring. For the *Pnma* phase at 500 K (Figure 6c), there is a clear long-range diffusion path along the *z*-direction between the Wyckoff 8*d1* and 8*d2* sites. Even though jumps between the 8*d1*–8*d1* and 8*d2*–8*d2* sites in the *xy*-plane are also possible, the relative amount of these jumps is lower compared to the relative amount of jumps between the 8*d1*–8*d2* site within the time simulated at all temperatures (between 4% and 31%, Table S4, Supporting Information). Thus the jumps along the *z*-direction have a lower activation energy than cross-plane jumps, indicating that the high conductivity is mainly but not exclusively due to these 1D diffusion pathways. For the *P-3m1* phase, the jumps along the *z*-direction are between the 6*h* and 6*g* sites and occur about equally often (39.3–51.6%) as jumps between the same Wyckoff sites (48.4–60.7%) (Figure 6d; Table S4, Supporting Information). The jumps around the hexagon appear to happen frequently (thick red lines) whereas the jumps to connect the hexagons happen rarely (no lines or very thin red lines). A different initial arrangement of Ho on the sites would lead to different diffusion pathways,[6,45] but this was not investigated in the scope of this report and was extensively studied in Schlem et al.[45] The study shows that disorder between the M1(*1a*) and M2(*2d*), which can be introduced by mechanochemical synthesis, increases the ionic conductivity in the *P-3m1* phase (in the simulations here, the M1(*1a*) and M2(*2d*) were large, therefore a conductive version of the *P-3m1* phase was simulated). The increase in ionic conductivity is rationalized by two simultaneous mechanisms. One is the different M(III) distribution leading to a redistribution of the Li atoms, which is more favorable. This is accompanied by an increase in the triangular area of face sharing octahedra/tetrahedra, which increases the size of the bottleneck.[45] Considering that both the *Pnma* and *P-3m1* phase consist of hexagonal close packing of the chlorine atoms, the difference between the two phases essentially is the different cation distribution, hence the rationale here is similar to their first mechanism. The diffusion in the *z*-direction, which is very fast according to the ab initio simulations here, corresponds to jumps between face sharing octahedra, while the diffusion in the *xy*-plane is diffusion between face sharing oct–tet–oct path. The results therefore indicate that the M(III) distribution in the *Pnma* phase favors jumps between face-sharing octahedras, which, considering the higher tracer diffusivity, is a faster path than the oct–tet–oct path in the *xy*-plane.

2.5. Electrochemical Studies

The electrochemical stability window of $Li_{2.73}Ho_{1.09}Cl_6$ is predicted to be 0.64–4.25 V (Figure S21a, Supporting Information) by using the established scheme based on the Material

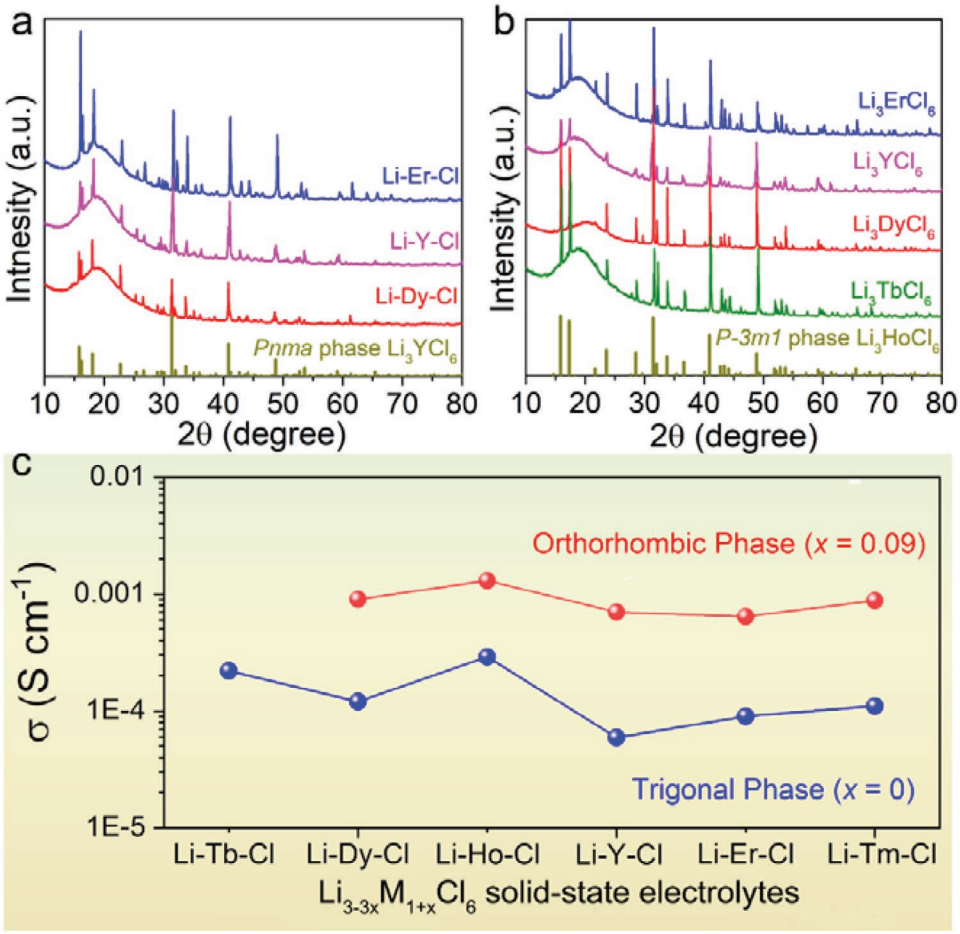

Figure 5. a) XRD patterns of the $Li_{2.73}M_{1.09}Cl_6$ ($x = 0.09$, M = Er, Y, Dy, *Pnma* phase). b) XRD patterns of the Li_3MCl_6 ($x = 0$, M = Er, Y, Dy, Tb, *P-3m1* phase). c) The RT ionic conductivities of the $Li_{3-3x}Ho_{1+x}Cl_6$ SSEs.

project,[46] which is further reflected from the cyclic voltammetry test of the $Li/Li_7P_3S_{11}/Li_{2.73}Ho_{1.09}Cl_6/Li_{2.73}Ho_{1.09}Cl_6$–Au cell (Figure S21b, Supporting Information). The stability of $Li_{2.73}Ho_{1.09}Cl_6$ toward bare Li metal was evaluated by galvanostatic cycling at 0.1 mA cm^{-2} (0.5 mAh cm^{-2}) and EIS at RT (Figures S21c–S23, Supporting Information), which indicates that side reaction between Li metal and $Li_{2.73}Ho_{1.09}Cl_6$ occurred, while the overall interfacial resistance can be dynamically stable over a period of time. Thus, the performance of $Li_{2.73}Ho_{1.09}Cl_6$ as SSE in ASSLBs is demonstrated with a composite cathode with $LiNi_{0.8}Mn_{0.1}Co_{0.1}O_2$ (NMC811) as active materials (NMC811/$Li_{2.73}Ho_{1.09}Cl_6$ = 7:3, w/w) and In as anode. **Figure 7**a presents the charge/discharge profiles of the ASSLB operated at 25 °C and –10 °C. At 25 °C, the initial charge/discharge capacities are 209 and 172 mAh g^{-1} (0.1 C, 1 C = 200 mA g^{-1}), corresponding to an initial Coulombic efficiency of 82.3%. At –10 °C, the NMC811/$Li_{2.73}Ho_{1.09}Cl_6$/In ASSLB exhibits an initial Coulombic efficiency of 79.4% and a reversible capacity of 142 mAh g^{-1} at 0.025 C, which might be caused by the sluggish Li^+ migration within the cathode layer at a lower temperature. The NMC811/$Li_{2.73}Ho_{1.09}Cl_6$/In ASSLBs show good cycling performance at both temperatures (Figure 7b; Figure S24, Supporting Information), with specific capacities of 125.5 and 90 mAh g^{-1} remaining after 180 cycles (25 °C) and 100 cycles at –10 °C. The typical delithiation/lithiation behavior of NMC811 is clearly visible in the differential capacity curves (Figure 7c). The rate capabilities at different current densities ranging from 20 to 200 mA g^{-1} (0.1 C to 1 C) at 25 °C are displayed in Figure 7d. The capacity gradually decreases along with an increase of current density, with 98 mAh g^{-1} achieved at 1 C (58% capacity retention of that at 0.1 C). The capacity can be recovered upon returning to the initial 0.1 C rate. The in situ EIS spectra in Figure 7e show that the mid-frequency semicircle related to the NMC811/$Li_{2.73}Ho_{1.09}Cl_6$ interfacial resistance increased slightly during the charging process and decreased again during the discharging process, which might be caused by the mild volume shrinkage of NMC811 during delithiation and corresponding volume recovery once lithiated.[47] Synchrotron-based high energy X-ray photoelectron spectra (HEXPS) of NMC811/$Li_{2.73}Ho_{1.09}Cl_6$ composites at different states (Figure 7f,g; Figure S25, Supporting Information) remain the same, indicating that there is a stable interface between NMC811 and $Li_{2.73}Ho_{1.09}Cl_6$ regardless of the static physical contact or during the charge/discharge cycling process. Such conclusion can be further supported by the Ho L_3-edge XANES spectra (Figure 7h) and the corresponding first derivative spectra (Figure 7i) of the

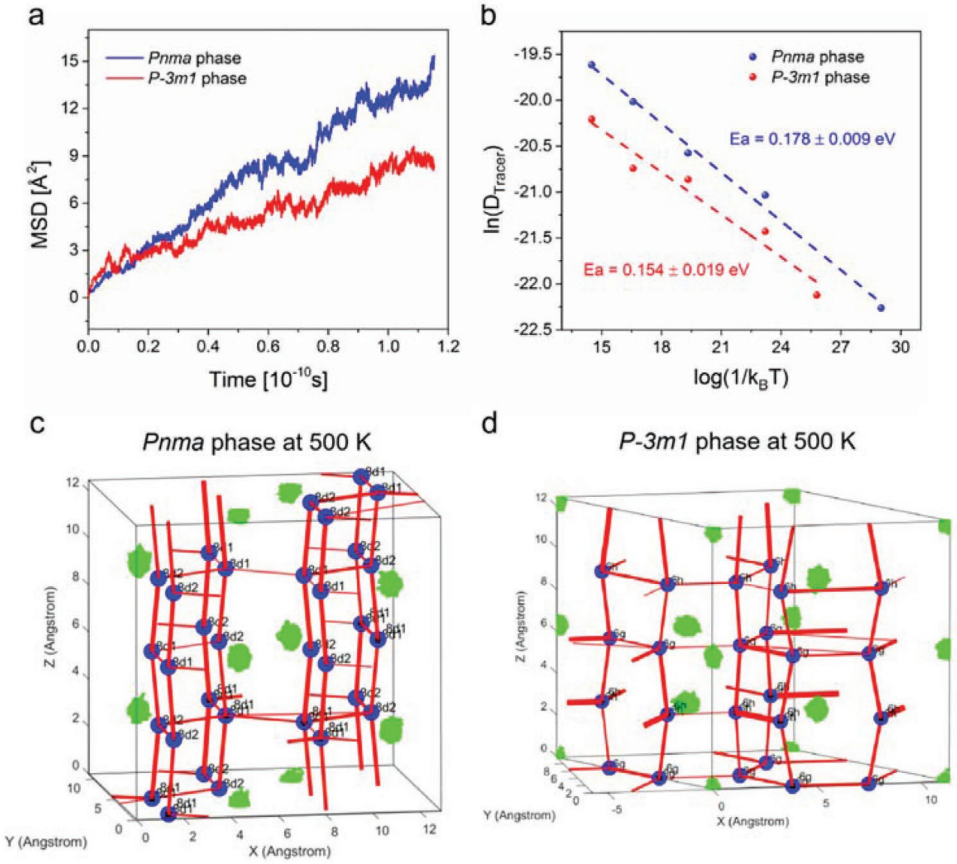

Figure 6. a) Mean squared displacement (MSD) of the *P-3m1* and *Pnma* phase at 600 K as a function of the simulation time (the *P-3m1* phase was run longer than shown here). For the total MSD per simulation, see Figure S15 of the Supporting Information. b) Logarithm of the Tracer diffusion coefficient versus $1/k_bT$ for different temperatures. The ionic jumps between different Li sites in c) *Pnma* phase and d) *P-3m1* phase at 500 K. The Li-sites (blue), Ho-trajectories (green), and Li-ion jumps that occurred during the simulation (red). The size of the Li-sites and the thickness of the Lines represent the occupancy of the site during the simulation and the jump frequency, respectively.

NMC811/$Li_{2.73}Ho_{1.09}Cl_6$ composite at different charge/discharge states.

3. Conclusions

In summary, the ternary metal chloride solid electrolyte series of $Li_{3-3x}M_{1+x}Cl_6$ ($-0.14 < x \leq 0.2$, M = Tb, Dy, Ho, Y, Er, Tm) reveal a phase transition from trigonal *(P-3m1)* to orthorhombic (*Pnma*) upon increasing x values. Both *P-3m1* and *Pnma* structures consist of the hcp framework of Cl^- anions but differ in their cations (including Li^+ and M^{3+}) arrangement. Using $Li_{3-3x}Ho_{1+x}Cl_6$ ($-0.14 < x \leq 0.2$) as an example, the relationship between structure and Li-ion conductivity is revealed by temperature-dependent EIS, X-ray and neutron diffractions, and ab initio molecular dynamics (MD) simulations. The highest RT Li^+ conductivity of 1.3×10^{-3} S cm^{-1} is achieved for the orthorhombic $Li_{2.73}Ho_{1.09}Cl_6$ sample, which is over four times higher than that of the trigonal Li_3HoCl_6 (0.3×10^{-3} S cm^{-1}). About one order of magnitude difference in ionic conductivities is observed in the isostructural Li–Dy–Cl, Li–Y–Cl, Li–Er–Cl, and Li–Tm–Cl composites. The phase transition to *Pnma* triggers a significant increase in Li^+ diffusivity and reduces the activation energy barrier for Li^+ diffusion in all different Li–M–Cl systems. Ab initio MD simulations consistently derive a higher diffusivity and reduced activation energy of the *Pnma* phase due to the facile diffusion in the *z*-direction compared to the *P-3m1* phase. The synthesis strategy based on trigonal-to-orthorhombic phase transition phenomenon not only can be used to discover the fundamental chemical theories of the rare earth metal halides but also can explore new materials with high Li^+ conductivity. All-solid-state batteries of NMC811/$Li_{2.73}Ho_{1.09}Cl_6$/In exhibit excellent electrochemical performances at both RT and low temperature. These results provide guidance for the design of novel halide superionic conductors and contribute to the development of ASSLBs.

4. Experimental Section

Preparation of the $Li_{3-3x}M_{1+x}Cl_6$: All preparations and sample treatments were carried out under argon atmosphere (O_2 < 1 ppm, H_2O < 1 ppm). The $Li_{3-3x}M_{1+x}Cl_6$ (M = Tb, Dy, Ho, Y, Er, Tm) SSEs were synthesized using the following procedure: the starting materials of lithium chloride (LiCl, Alfa Aesar, 99.9%) and trivalent rare earth chloride (MCl_3, Alfa Aesar, >99.9%) were weighted in the appropriate stoichiometric ratio and directly put into quartz tubes. The quartz tubes

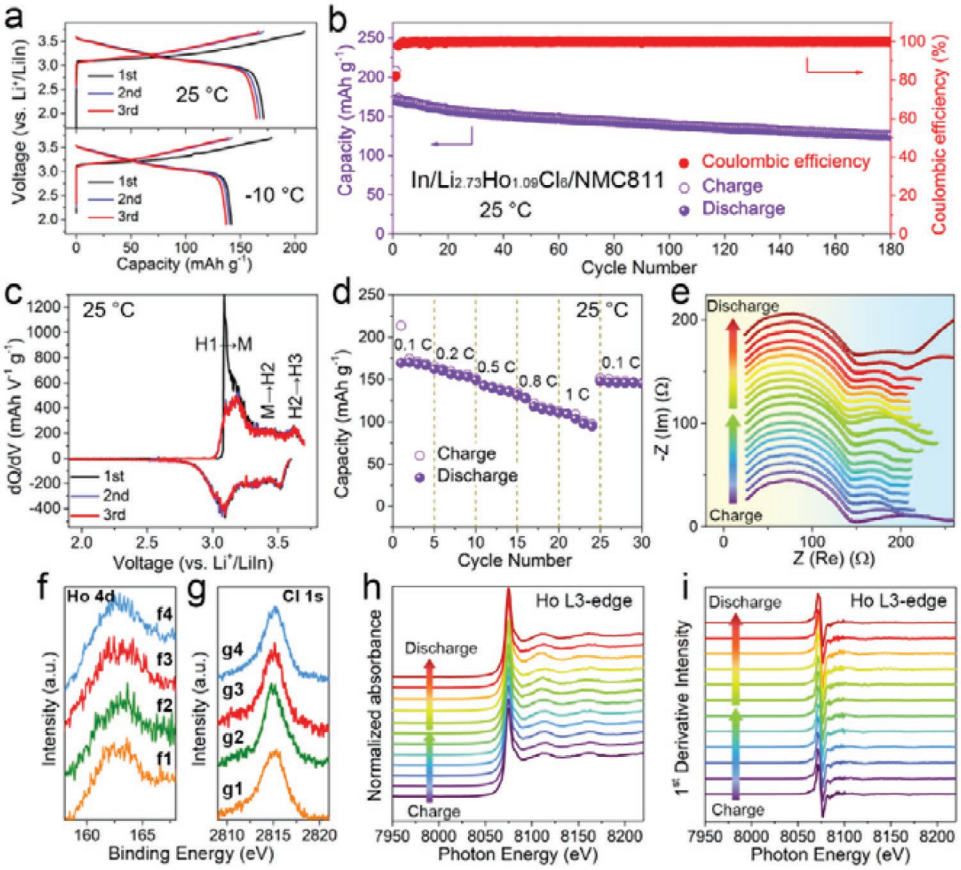

Figure 7. Electrochemical performance of NMC811/$Li_{2.73}Ho_{1.09}Cl_6$/In ASSLBs. a) The charge/discharge curves and b) the cycling performance recorded at 25 °C (0.1 C). c) The d*Q*/d*V* curves for the first three cycles at 0.1 C at 25 °C. d) Rate capability at 0.1, 0.2, 0.5, 0.8, and 1 C at 25 °C. e) EIS spectra of NMC811/$Li_{2.73}Ho_{1.09}Cl_6$/In ASSLB carried out after 2 h of charge/discharge and 2 h of rest. f,g) HEXPS of Ho 4d and Cl 1s spectra of NMC811-$Li_{2.73}Ho_{1.09}Cl_6$ cathode at a photon energy of 3000 eV recorded at different charge/discharge states, i.e., (f1,g1) pristine, (f2,g2) after first charge, (f3,g3) after the first discharge, and (f4,g4) fully discharged after 50 cycles. Ex situ h) Ho L_3-edge and i) the first derivatives of Ho L_3-edge XANES spectra of NMC811-$Li_{2.73}Ho_{1.09}Cl_6$ cathode composites at different charge–discharge states.

were sealed and heated to 650 °C (4 h heating), annealed for 24 h, and then cooled to room temperature.

Preparation of the LPO-Coating NMC811 Cathode: The NMC811 cathode was obtained from China Automotive Battery Research Institute Co. Ltd, China. The Li_3PO_4 thin layer was deposited on the surface of NMC811 using trimethyl phosphate (TMPO) and lithium tertbutoxide (LiOtBu) as precursors by atomic layer deposition (ALD, Cam-bridge Nanotech, USA). The deposition temperature for Li_3PO_4 thin layer was set at 250 °C. TMPO and LiOtBu were alternatively introduced into the reaction chamber with a pulse time of 2 s, and the pulsing of each precursor was separated by a 15 s in 1 cycle. The thickness of the Li_3PO_4 thin layer was controlled around 10 nm (100 cycles).

Characterizations: Powder XRD measurements of $Li_{3-3x}M_{1+x}Cl_6$ (M = Tb, Dy, Ho, Y, Er, Tm) were carried out on a Bruker AXS D8 Advance with a Cu Kα radiation (λ = 1.54178 Å). All samples were placed into a special holder to avoid possible air exposure during the test. Air stable performance was performed in a lithium battery dry room with a supply dew point around −50 °C and humidity around 1%. High-energy X-ray photoelectron spectroscopy of NMC811-$Li_{2.73}Ho_{1.09}Cl_6$ cathode at different charge/discharge states was carried on the soft X-ray microcharacterization beamline (SXRMB) in Canadian Light Source (CLS) under different energies. Holmium (Ho) XAFS data were measured at Hard X-ray MicroAnalysis (HXMA) beamline in CLS.

Neutron Diffraction: The time of flight powder neutron diffraction patterns were collected on the high-flux medium resolution diffractometer Polaris at ISIS,[48] Rutherford Appleton Laboratory, United Kingdom. 1.575 g of $Li_{2.73}Ho_{1.09}Cl_6$ powder was loaded into a 6 mm diameter thin-walled cylindrical vanadium can and sealed with an indium wire inside the glovebox. The sample was mounted in the diffractometer and data were collected at room temperature for a duration of 400 µAh integrated proton beam current to the ISIS neutron target (corresponding to ≈2 h total exposure). Data reduction and generation of files suitable for profile refinement used the Mantid open-source software.[49] The data were analyzed with the Rietveld refinement program GSAS-2 software.[50] As an initial guess, the structure file of the *Pnma* phase of Li_3YCl_6 was used, and Y was replaced by Ho. The lattice parameter and atomic positions were refined first, followed by sample broadening effects due to crystallite size. Instrument parameters were refined for small corrections in the time of flight due to sample placement and wavelength-dependent average penetration depth. The chlorine occupancies were fixed to 1, the holmium and the lithium occupancies were refined, where the lithium occupancy of the 8*d1* site (see Table S2, Supporting Information) was fixed to 1, while the Li 8*d2* and the Ho 4*c* site occupancies were refined but constrained to charge compensation. Both ^6Li and ^{165}Ho are strong neutron absorbers. This led to differences in the peak intensity for the same peaks measured on different banks. As the absorption affects peaks at a longer time of flight (larger *d*-spacing) more strongly, not the full measured range of each bank was used for the profile refinement. Instead, the peaks of the *d*-spacing range were taken into account for using the data of the next

bank, which has a somewhat lower resolution, but the longer *d*-spacing occurs at a shorter time of flight, avoiding the absorption problem at the cost of somewhat lower resolution. It was made sure that there was sufficient (almost complete) overlap between the banks, to ensure intensities were not fit solely because of the histogram scale parameter. Even with this strategy, due to the size of the unit cell, only banks 5, 4, and 3 were needed for the structure refinement. The background was modeled by a Chebyschev function with eight components.

Conductivity Measurements: Cold-pressed pellets (diameter of 10 mm, ≈380 MPa) were attached with carbon on both sides and then sealed in custom-built Model Cells for EIS tests. Ionic conductivity measurements were carried out in the temperature range from 258 to 338 K using a versatile multichannel potentiostat 3/Z (VMP3) impedance analyzer in the range of 7 MHz to 1 Hz with an amplitude of 10 mV. The activation energies of the $Li_{3-3x}M_{1+x}Cl_6$ samples were determined according to the Arrhenius equation of $\sigma T = \sigma_0 \exp(-E_a/k_B T)$, where σ, T, σ_0, E_a, and k_B are the ionic conductivity, the temperature in K, the pre-exponential factor, the activation energy, and the Boltzmann constant, respectively. The electronic conductivities of the samples were calculated by the Ohm's law of $\sigma_e = I_e \times L/(V \times A)$, where σ_e, I_e, L, V, and A is the electronic conductivity, the equilibrium current, the thickness of the SSE, the applied voltage, and the area of the SSE pellet, respectively.

MD Simulations: Density functional theory calculations were performed in VASP[51–53] using the GGA approximation[54] and the PAW-PBE basis set.[55,56] A 1 × 1 × 2 supercell was used, which results in a size of 80 atoms (12.89 × 11.21 × 12.45) for the *Pnma* phase and 60 atoms (11.33 × 9.76 × 12.45) for *P-3m1*. For both structures, cut-off energy of 450 eV and a k-point mesh of 2 × 2 × 2 was used for the relaxation as well as the molecular dynamics simulation. The values were chosen based on the convergence test of the total energy. The MDs were performed in the NVT ensemble, with a time step of 2 fs and an equilibration time of 2.5 ps for all simulations. The simulations were run for a different length depending on the phase and temperature, to reach a certain amount of jumps also at lower temperatures and for the less conducting phase. The output of the MD simulations was analyzed using the code published elsewhere.[44]

Structure generation for the (MD) Simulations: For the *P-3m1* phase, the cif file published in Bohnsack et al.[18] was used as a starting structure. The Ho partial occupancies were changed to 80% (from 97%) and 20% (from 3%), due to computational limitations concerning the size of the supercell and the refinement result of the *P-3m1* phase Li_3HoCl_6 sample. The partial occupancies of both Li and Ho lead to very many possible configurations in the supercell. Therefore, the ten structures with the lowest Ewald-sum of the configurational space were selected as implemented in Pymatgen.[57] After minimization without symmetry restrictions, the lowest energy configuration of the ten structures was selected for the MD simulations. For the *Pnma* phase, the cif file for Li_3YCl_6[18] was used as a starting structure. The partial occupancy was accommodated by placing Li-atoms on their sites so that the Li–Li distances are maximized. Ten structures were then relaxed without symmetry restrictions and the lowest energy configuration was used as starting point for the MDs.

Electrochemical Characterizations: All-solid-state batteries preparation processes were conducted inside an Ar-filled glove box. There was no liquid electrolyte used during the battery assembly process. The configuration of the solid-state batteries was a homemade model cell, with solid electrolyte, cathode composite, and In foil anode pressed into the cell layer by layer using stainless-steel terminals and hydraulic press. The electrochemical stability was evaluated by cyclic voltammetry (CV) measurements using a versatile multichannel potentiostat 3/Z (VMP3) with a $Li/Li_3PS_4/Li_{3-3x}Ho_{1+x}Cl_6/Li_{3-3x}Ho_{1+x}Cl_6$–Au cell in a scanning range of –0.2 to 5 V (vs Li/Li^+) at 0.1 mV s^{-1}. The active $Li_{3-3x}Ho_{1+x}Cl_6$–Au layer was prepared by mixing Au and $Li_{3-3x}Ho_{1+x}Cl_6$ with a mass ratio of 1:1. Symmetrical all-solid-state $Li/Li_{3-3x}Ho_{1+x}Cl_6/Li$ cells were assembled with bare Li metal as the electrodes and cold-pressed $Li_{3-3x}Ho_{1+x}Cl_6$ pellet as the solid-state electrolyte layer. Commercial $LiNi_{0.8}Mn_{0.1}Co_{0.1}O_2$ (NMC811) with a 5 nm Li_3PO_4 coating by ALD without infusion was used as the cathode active material.[58] For the preparation of cathode composites, NMC811 and as-prepared $Li_{3-3x}Ho_{1+x}Cl_6$ SSEs with a mass ratio of 7:3 were ground together in an agate mortar for 10 min. 80 mg of the as-synthesized $Li_{3-3x}Ho_{1+x}Cl_6$ was compressed at 2 tons to form a solid-state electrolyte layer. Approximately 10 mg of cathode composite was then spread on one side of the $Li_{3-3x}Ho_{1+x}Cl_6$ pellet and further pressed at 3 tons (≈380 MPa). The diameter of the pallet was 1 cm. Then a piece of In foil was put on the other side of the $Li_{3-3x}Ho_{1+x}Cl_6$ and pressed at 1 ton (≈125 MPa). The cells were cycled in the voltage range of 1.9–3.7 V (vs Li^+/Li–In) by using the homemade model cells and a Land cycler (Wuhan, China) at room temperature and –10 °C.

Supporting Information

Supporting Information is available from the Wiley Online Library or from the author.

Acknowledgements

J.L., E.v.d.M., and J.L. contributed equally to this work. This research was supported by the Natural Sciences and Engineering Research Council of Canada (NSERC), Canada Research Chair Program (CRC), Canada Foundation for Innovation (CFI), GLABAT Solid-State Battery Inc., China Automotive Battery Research Institute Co. Ltd, Ontario Research Fund, the Canada Light Source at University of Saskatchewan (CLS), Interdisciplinary Development Initiatives (IDI) by Western University, Canada MITACS fellow, and University of Western Ontario. Financial support was greatly acknowledged from the Netherlands Organization for Scientific Research (NWO) under the VICI Grant No. 16122. The authors also appreciate the help of the beamline scientist of HXMA (Dr. Weifeng Chen) and SXRMB (Dr. Mohsen Shakouri, Dr. Qunfeng Xiao, and Dr. Alisa Paterson) beamline at Canadian Light Source. The authors thank the UK Science and Technology Facilities Council (STFC) for provision of Xpress Access neutron beamtime at ISIS.[59]

Conflict of Interest

The authors declare no conflict of interest.

Data Availability Statement

The data that support the findings of this study are available from the corresponding author upon reasonable request.

Keywords

all-solid-state Li batteries, energy storage, halides, solid-state electrolytes, superionic conductors

Received: December 14, 2021
Revised: February 21, 2022
Published online:

[1] T. Famprikis, P. Canepa, J. Dawson, M. Islam, C. Masquelier, *Nat. Mater.* **2019**, *18*, 1278.
[2] Z. Zhang, Y. Shao, B. Lotsch, Y. Hu, H. Li, J. Janek, L. Nazar, C. Nan, J. Maier, M. Armand, L. Chen, *Energy Environ. Sci.* **2018**, *11*, 1945.

[3] R. Chen, Q. Li, X. Yu, L. Chen, H. Li, *Chem. Rev.* **2020**, *120*, 6820.
[4] M. Weiss, F. Simon, M. Busche, T. Nakamura, D. Schröder, F. Richter, J. Janek, *Electrochem. Energy Rev.* **2020**, *3*, 221.
[5] Q. Zhao, S. Stalin, C. Zhao, L. Archer, *Nat. Rev. Mater.* **2020**, *5*, 229.
[6] X. Li, J. Liang, X. Yang, K. Adair, C. Wang, F. Zhao, X. Sun, *Energy Environ. Sci.* **2020**, *13*, 1429.
[7] R. Schlem, T. Bernges, C. Li, M. Kraft, N. Minafra, *ACS Appl. Energy Mater.* **2020**, *3*, 3684.
[8] Q. Zhang, D. Cao, Y. Ma, A. Natan, P. Aurora, H. Zhu, *Adv. Mater.* **2019**, *31*, 1901131.
[9] S. Ohno, A. Banik, G. F. Dewald, M. A. Kraft, T. Krauskopf, N. Minafra, P. Till, M. Weiss, W. G. Zeier, *Prog. Energy* **2020**, *2*, 022001.
[10] Y. Liu, S. Wang, A. M. Nolan, C. Ling, Y. Mo, *Adv. Energy Mater.* **2020**, *10*, 2002356.
[11] S. Wang, Q. Bai, A. M. Nolan, Y. Liu, S. Gong, Q. Sun, Y. Mo, *Angew. Chem., Int. Ed.* **2019**, *58*, 8039.
[12] Y. Zhu, Y. Mo, *Angew. Chem., Int. Ed.* **2020**, *59*, 17472.
[13] D. Park, H. Park, Y. Lee, S. O. Kim, H. G. Jung, K. Y. Chung, J. H. Shim, S. Yu, *ACS Appl. Mater. Interfaces* **2020**, *12*, 34806.
[14] T. Asano, A. Sakai, S. Ouchi, M. Sakaida, A. Miyazaki, S. Hasegawa, *Adv. Mater.* **2018**, *30*, 1803075.
[15] H. J. Steiner, H. D. Lutz, *Z. Anorg. Allg. Chem.* **1992**, *613*, 26.
[16] E. J. Plichta, W. K. Behl, D. Vujic, W. H. S. Chang, D. M. Schleich, *J. Electrochem. Soc.* **1992**, *139*, 1509.
[17] R. Kanno, Y. Takeda, O. Yamamoto, *Mater. Res. Bull.* **1981**, *16*, 999.
[18] A. Bohnsack, F. Stenzel, A. Zajonc, G. Balzer, M. S. Wickleder, G. Meyer, *Z. Anorg. Allg. Chem.* **1997**, *623*, 1067.
[19] X. Li, J. Liang, J. Luo, M. N. Banis, C. Wang, W. Li, S. Deng, C. Yu, F. Zhao, Y. Hu, T. Sham, L. Zhang, S. Zhao, S. Lu, H. Huang, R. Li, K. R. Adair, X. Sun, *Energy Environ. Sci.* **2019**, *12*, 2665.
[20] X. Li, J. Liang, N. Chen, J. Luo, K. R. Adair, C. Wang, M. N. Banis, T. K. Sham, L. Zhang, S. Zhao, S. Lu, H. Huang, R. Li, X. Sun, *Angew. Chem., Int. Ed.* **2019**, *58*, 16427.
[21] K. H. Park, K. Kaup, A. Assoud, Q. Zhang, X. Wu, L. F. Nazar, *ACS Energy Lett.* **2020**, *5*, 533.
[22] X. Li, J. Liang, K. R. Adair, J. Li, W. Li, F. Zhao, Y. Hu, T. K. Sham, L. Zhang, S. Zhao, S. Lu, H. Huang, R. Li, N. Chen, X. Sun, *Nano Lett.* **2020**, *20*, 384.
[23] J. Liang, X. Li, S. Wang, K. R. Adair, W. Li, Y. Zhao, C. Wang, Y. Hu, L. Zhang, S. Zhao, S. Lu, H. Huang, R. Li, Y. Mo, X. Sun, *J. Am. Chem. Soc.* **2020**, *142*, 7012.
[24] L. Zhou, C. Y. Kwok, A. Shyamsunder, Q. Zhang, X. Wu, L. F. Nazar, *Energy Environ. Sci.* **2020**, *13*, 2056.
[25] H. Kwak, D. Han, J. Lyoo, J. Park, S. H. Jung, Y. Han, G. Kwon, H. Kim, S. T. Hong, K. W. Nam, Y. S. Jung, *Adv. Energy Mater.* **2021**, *11*, 2003190.
[26] S. Y. Kim, K. Kaup, K. H. Park, A. Assoud, L. Zhou, J. Liu, X. Wu, L. F. Nazar, *ACS Mater. Lett.* **2021**, *3*, 930.
[27] J. Park, D. Han, H. Kwak, Y. Han, Y. J. Choi, K. W. Nam, Y. S. Jung, *Chem. Eng. J.* **2021**, *425*, 130630.
[28] R. Schlem, A. Banik, S. Ohno, E. Suard, W. G. Zeier, *Chem. Mater.* **2021**, *33*, 327.
[29] M. Gombotz, H. M. R. Wilkening, *ACS Sustainable Chem. Eng.* **2020**, *9*, 743.
[30] L. M. Riegger, R. Schlem, J. Sann, W. G. Zeier, J. Janek, *Angew. Chem.* **2021**, *133*, 6792.
[31] Z. Liu, S. Ma, J. Liu, S. Xiong, Y. Ma, H. Chen, *ACS Energy Lett.* **2020**, *6*, 298.
[32] Y. Fu, C. Ma, *Sci. China Mater.* **2021**, *64*, 1378.
[33] B. Helm, R. Schlem, B. Wankmiller, A. Banik, A. Gautam, J. Ruhl, C. Li, M. R. Hansen, W. G. Zeier, *Chem. Mater.* **2021**, *33*, 4773.
[34] B. Zahiri, A. Patra, C. Kiggins, A. X. B. Yong, E. Ertekin, J. B. Cook, P. V. Braun, *Nat. Mater.* **2021**, *20*, 1392.
[35] J. Liang, X. Li, K. R. Adair, X. Sun, *Acc. Chem. Res.* **2021**, *54*, 1023.
[36] Y. Xiao, Y. Wang, S. H. Bo, J. C. Kim, L. J. Miara, G. Ceder, *Nat. Rev. Mater.* **2020**, *5*, 105.
[37] S. Muy, J. Voss, R. Schlem, R. Koerver, S. J. Sedlmaier, F. Maglia, P. Lamp, W. G. Zeier, Y. Shao-Horn, *iScience* **2019**, *26*, 270.
[38] J. J. Rehr, R. C. Albers, *Rev. Mod. Phys.* **2000**, *72*, 621.
[39] Y. Joly, *Phys. Rev. B* **2001**, *63*, 125120.
[40] A. K. Jonscher, *Nature* **1977**, *267*, 673.
[41] A. K. Jonscher, *J. Mater. Sci.* **1981**, *16*, 2037.
[42] G. J. Brug, A. L. G. Van Den Eeden, M. Sluyters-Rehbach, J. H. Sluyters, *J. Electroanal. Chem.* **1984**, *176*, 275.
[43] J. T. S. Irvine, D. C. Sinclair, A. R. West, *Adv. Mater.* **1990**, *2*, 132.
[44] N. J. J. de Klerk, E. van der Maas, M. Wagemaker, *ACS Appl. Energy Mater.* **2018**, *1*, 3230.
[45] R. Schlem, S. Muy, N. Prinz, A. Banik, Y. Shao-Horn, M. Zobel, W. G. Zeier, *Adv. Energy Mater.* **2019**, *10*, 1903719.
[46] A. Jain, S. P. Ong, G. Hautier, W. Chen, W. D. Richards, S. Dacek, S. Cholia, D. Gunter, D. kinner, G. Ceder, *APL Mater.* **2013**, *1*, 011002.
[47] K. Raimund, W. Zhang, L. de Biasi, S. Schweidler, A. O. Kondrakov, S. Kolling, T. Brezesinski, P. Hartmann, W. G. Zeier, J. Janek, *Energy Environ. Sci.* **2018**, *11*, 2142.
[48] R. I. Smith, S. Hull, M. G. Tucker, H. Y. Playford, D. J. McPhail, S. P. Waller, S. T. Norberg, *Rev. Sci. Instrum.* **2019**, *90*, 115101.
[49] O. Arnold, J. C. O. Bilheux, J. M. Borreguero, A. Buts, S. I. Campbell, L. Chapon, M. Doucet, N. Draper, R. F. Leal, M. A. Gigg, V. E. Lynch, *Nucl. Instum. Methods Phys. Res.* **2014**, *A764*, 156.
[50] B. H. Toby, R. B. Von Dreele, *J. Appl. Cryst.* **2013**, *46*, 544.
[51] G. Kresse, J. Hafner, *Phys. Rev. B* **1993**, *47*, 558.
[52] G. Kresse, J. Furthmüller, *Comput. Mater. Sci.* **1996**, *6*, 15.
[53] G. Kresse, J. Furthmüller, *Phys. Rev. B* **1996**, *54*, 11169.
[54] J. P. Perdew, K. Burke, M. Ernzerhof, *Phys. Rev. Lett.* **1996**, *77*, 3865.
[55] G. Kresse, J. Hafner, *J. Phys.: Condens. Matter* **1994**, *6*, 8245.
[56] G. Kresse, D. Joubert, *Phys. Rev. B* **1999**, *59*, 1758.
[57] S. P. Ong, W. D. Richards, A. Jain, G. Hautier, M. Kocher, S. Cholia, D. Gunter, V. L. Chevrier, K. A. Persson, G. Ceder, *Comput. Mater. Sci.* **2013**, *68*, 314.
[58] S. Deng, X. Li, Z. Ren, W. Li, J. Luo, J. Liang, J. Liang, M. N. Banis, M. Li, Y. Zhao, X. Li, C. Wang, Y. Sun, Q. Sun, R. Li, Y. Hu, L. Zhang, S. Lu, J. Luo, X. Sun, *Energy Storage Mater.* **2020**, *27*, 117.
[59] S. Parnell, Battery Material Candidates Sample 1, STFC ISIS Neutron and Muon Source, **2020**, https://doi.org/10.5286/ISIS.E.RB1990349-1.